



Multiple mechanisms for chlorophyll-a concentration variations in coastal upwelling regions: A case study east of Hainan Island in the South China Sea

Junyi Li^{1,2,3}, Min Li^{1*}, Chao Wang¹, Quanan Zheng^{1,4}, Ying Xu³, Tianyu Zhang¹, Lingling Xie^{1*}

¹ Laboratory of Coastal Ocean Variation and Disaster Prediction, Guangdong Ocean University, Zhanjiang 524088, China

² Key Laboratory of Climate, Sources and Environments in Continent Shelf Sea and Deep Ocean, Zhanjiang 524088, China

³ Key Laboratory of Space Ocean Remote Sensing and Application, MNR, Beijing, 100081, China

⁴ Department of Atmospheric and Oceanic Science, University of Maryland, College Park, MD 20742, USA

Corresponding author.

E-mail address: M. Li (min_li@gdou.edu.cn), L. Xie (xiell@gdou.edu.cn);

Abstract

Using satellite observations from 2003 to 2020 and cruise observations in 2019 and 2021, this study reveals an unexpected minor role of upwelling in seasonal and interannual variations in chlorophyll-a (Chl-a) concentrations in the coastal upwelling region east of Hainan Island (UEH) in the northwestern South China Sea (NWSCS). The results show strong seasonal and interannual variability in the Chl-a concentration in the core upwelling area of the UEH. Different from the strongest upwelling in summer, the Chl-a concentration in the UEH area reaches a maximum of 1.18 mg m⁻³ in autumn and winter, with a minimum value of 0.74 mg m⁻³ in summer. The summer Chl-a concentration increases to as high as 1.0 mg m⁻³ with weak upwelling during El Niño years, whereas the maximum Chl-a concentration in October increases to 2.5 mg m⁻³ during La Niña years. The analysis of environmental factors shows that compared to the limited effects of upwelling, the along-shelf coastal current from the northern shelf and the increased precipitation are crucially important to the Chl-a concentration variation in the study area. These results provide new insights for predicting marine productivity in upwelling areas, i.e., multiple mechanisms, especially horizontal advection, should be considered in addition to the upwelling process.

Keywords: Coastal upwelling; chlorophyll-a concentration; Guangdong Coastal Current; ENSO events; EOF analysis

1 Introduction

The oceanic area with coastal upwelling is generally characterized by high productivity; it occupies only 1% of the total area of the ocean but provides more than 50% of the total marine fish harvest (Barua, 2005). High levels of biological productivity strongly influence atmosphere-ocean carbon recycling (Mcgregor et al., 2007; Xu et al., 2020). Therefore, revealing the variation in chlorophyll-a (Chl-a) in coastal upwelling areas is important to the overall health of the marine ecosystem and climate.

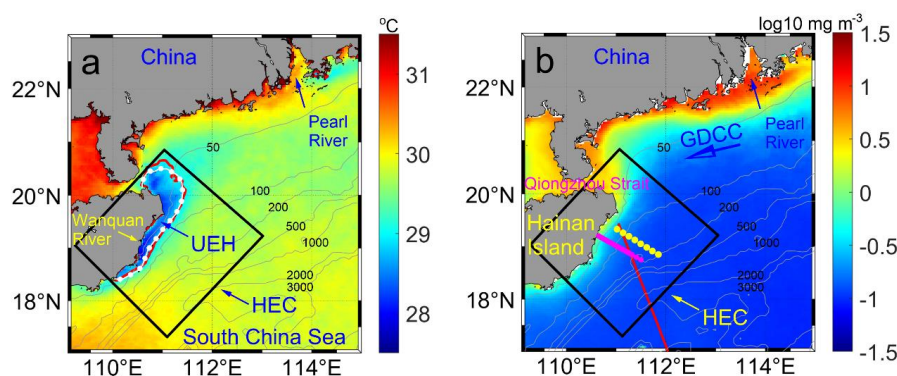
The upward movement of seawater may carry nutrients from the lower layer and support a high surface Chl-a concentration. Thus, the variability in Chl-a concentrations in coastal upwelling regions is proposed to be associated with that of upwelling (Jing et al., 2009). Alongshore winds, positive wind curl, tidal mixing and topography may affect upwelling processes (Hu and Wang,



2016). In contrast, other oceanic and atmospheric processes, such as mesoscale eddies, sub-
 mesoscale fronts, precipitation and typhoon processes, can also induce Chl-a increments (Aoki et
 al., 2019; Cape et al., 2019; Li et al., 2021a; Li et al., 2021b).

The coastal upwelling east of Hainan Island (UEH) is part of the seasonal upwelling in the
 northwestern South China Sea (NWSCS). As shown in Figure 1, the isobaths in the shelf are
 parallel to the continental coastline. The width of the continental shelf is approximately 100 km.
 Outside of the continental shelf, there is a steep slope linking the shelf to the South China Sea
 (SCS) Basin. The circulation in the coastal area east of Hainan Island (HEC) is controlled by the
 East Asian monsoon system. In summer, the coastal current travels northeastward on the shelf
 influenced by the southwesterly monsoon, whereas in winter, the current flows southwestward
 (Ding et al., 2018; Jing et al., 2015). According to the Ekman transport theory, the along-shelf
 wind induces cross-shelf transport of the surface water and thus causes coastal upwelling along the
 coastline in summer. The UEH generally begins in April, becomes strongest in July and August,
 and remains until September (Xie et al., 2012). The UEH is located in coastal shallow water less
 than 100 m (Jing et al., 2015). Wind stress curl-induced Ekman pumping is considered to be
 another crucial factor for UEH generation (Xu et al., 2020). In addition, the strong northeastward
 current along the shelf enhances upwelling (Su et al., 2013).

62



63

Figure 1. Study area (black solid square) and sampling sites. (a) Climatological (June–August) sea
 surface temperature (SST) and (b) Chl-a concentration during 2003–2020. In panel (a), the white
 dotted curve is the SST front for June–August; the red curve is the 29°C isotherm. In (b), the dots
 are the observation sites for the cruise during July 14–15, 2021 (yellow), and October 2–3, 2019
 (magenta), and the red curve is the altimeter satellite ground track (Track 114). The unit of the
 numbers on the isobaths is meters.

70

The variation in primary production in the HEC has been variously reported. Deng et al.
 (1995) reported that phytoplankton achieved a maximum value in a strong period of UEH. Jing et
 al. (2011) found a higher Chl-a concentration in summer 1998, as the offshore Ekman transport
 was the strongest. Southwesterly monsoon-induced coastal upwelling is suggested to be the major
 mechanism for the relatively high summertime phytoplankton biomass and primary production
 (Liu et al., 2013; Song et al., 2012). Moreover, Hu et al. (2021) found that eddy processes could
 strengthen phytoplankton blooms in the HEC. The variation in the basin circulation may also

77



78 affect the UEH (Su et al., 2013; Wang et al., 2006). However, Ning et al. (2004) reported poor
 79 nutrients, low Chl-a, and weak primary production in summer in the HEC. Shi et al. (2021) found
 80 that the largest Chl-a increase in the HEC occurs in May when upwelling is weak. Li et al. (2021a)
 81 further showed that the maximum Chl-a concentration year-round exhibits a double peak in March
 82 and October.

83 The results of previous studies indicate that upwelling may not be the most significant factor
 84 affecting primary productivity in the HEC (Li et al., 2021a; Ning et al., 2004). The mechanism
 85 driving the variation in primary productivity in the HEC thus needs further investigation.

86 The objective of this study is to reveal the role of upwelling in the spatial-temporal variations
 87 in Chl-a concentrations in the HEC area based on multi-sensor satellite observations and in situ
 88 cruise observations. The article is organized as follows. Section 2 describes the materials and
 89 methods, including the algorithms used for retrieval of the total suspended sediment (TSS) and sea
 90 surface temperature (SST) front from satellite observations. Section 3 presents the results and
 91 analysis of the spatial-temporal variations in the Chl-a concentration in the study area. Section 4
 92 presents variations in environmental factors in the study area, including monthly climatological
 93 wind, rainfall, SST, sea surface salinity (SSS), euphotic depth, and TSS. Section 5 discusses the
 94 role of typhoons, coastal currents, ENSO events, and precipitation in the Chl-a concentration.
 95 Section 6 presents the conclusions.

97 **2 Materials and methods**

98 **2.1 Study area and upwelling area**

99 The study area (enclosed by the black square in Figure 1) covers the UEH area off the
 100 northeastern coast of Hainan Island. It is adjacent to the narrow Qiongzhou Strait in the west and
 101 adjoins the wide continental shelf of the NWSCS in the east. The Wanquan River flowing through
 102 east Hainan Island is the third largest river on Hainan Island. The East Asian monsoon prevails in
 103 the HEC, and the UEH appears along the coast in summer (Lin et al., 2016). In fall and winter, a
 104 southwestward current flows along the coast on the whole shelf (Ding et al., 2018; Li et al., 2016).
 105 The nutrients in the Pearl River runoff can be transported to the HEC area by the Guangdong
 106 Coastal Current (GDCC). The thermal fronts stretch along the continental shelf (dotted white
 107 curve in Figure 1a) and are accompanied by high Chl-a concentrations (Figure 1b).

109 **2.2. Satellite observations and retrieval**

110 The monthly ocean color elements (Kd490, Rrs645, Chl-a, SST, and photosynthetically
 111 active radiation (PAR)) were obtained by moderate resolution imaging spectroradiometer
 112 (MODIS) instruments onboard the Terra and Aqua satellites. The dataset from 2003 to 2020 is a
 113 level-3 product with a spatial resolution of 4 km. The data from the two platforms were merged to
 114 improve the coverage of the Chl-a concentration (Li et al., 2021b). The TSS concentration was
 115 estimated from the Rrs645 product (Li et al., 2021b):

$$116 \quad C_{TSS} = 0.6455 + 1455.7 \times Rrs645 \quad (1)$$

117 The euphotic depth retrieval from the Kd490 product was conducted as follows (Zhao et al.,
 118 2013):

$$119 \quad Z_{eu} = 0.28 + \frac{395.92 \times 0.0092}{0.0092 + Kd490} \quad (2)$$



120 The surface thermal front was estimated using the SST gradient. The SST gradient was
 121 calculated using the zonal and meridional components ($GSST_x$, $GSST_y$) as follows:

$$122 \quad GSST = \sqrt{(GSST_x)^2 + (GSST_y)^2} \quad (3)$$

123 where $GSST_x = \left(\frac{SST_{i+1} - SST_{i-1}}{x_{i+1} - x_{i-1}} \right)$ ($^{\circ}\text{C}/\text{km}$), and $(x_{i+1} - x_{i-1})$ is equal to twice the spatial
 124 resolution.

125 The sea surface wind (SSW), sea surface wind stress, and wind stress curl at 10 m above the
 126 sea surface, with a spatial resolution of 0.25° , were obtained from the Copernicus Marine Service
 127 (CMEMS). The wind data from May 2007 to December 2020 used in this study were a monthly
 128 product, which was estimated from daily global wind fields calculated from retrievals derived
 129 from advanced scatterometers (ASCAT). The wind data from January 2003 to April 2020 were
 130 calculated from the daily global wind fields obtained by quick scatterometers (QuikSCATs).

131 A cross-shelf and along-shelf coordinate system for the SSW vector is given by:

$$132 \quad u_{\text{along}} = u \cos \theta - v \sin \theta \quad (4)$$

$$133 \quad v_{\text{cross}} = u \sin \theta + v \cos \theta \quad (5)$$

134 where the cross-shelf wind, v_{cross} , is seaward positive; the along-shelf wind, u_{along} , is southward
 135 parallel to the coastline; θ is the angle between the shoreline and the north direction, 25° in this
 136 study; and (u, v) are the east and north components of the SSW.

137 The monthly sea surface salinity (SSS) data from 2018 to 2020 with a spatial resolution of
 138 0.25° were obtained from the CMEMS.

139 The daily rainfall rate during 2003–2020 was obtained from the multi-satellite precipitation
 140 analysis dataset of the Tropical Rainfall Measuring Mission (TRMM). The monthly data with a
 141 spatial resolution of 0.25° were calculated from the daily global rainfall data.

142 The satellite altimeter along-track sea level anomaly (SLA) data from 2003 to 2020 were
 143 obtained from the CMEMS. The Jason-1, Jason-2, and Jason-3 satellites repeat their ground tracks
 144 every 9.9 d. Their sampling frequency is 1 Hz, and their spatial resolution is approximately 7 km.
 145 The 5-point moving average was applied to the along-track SLA data to filter out the small-scale
 146 ocean processes. As the coastline is almost perpendicular to ground track 114 of the altimeter
 147 satellites (Figure 1b), the along-shelf geostrophic current was estimated from the along-track SLA
 148 data as follows:

$$149 \quad u = -\frac{g}{f} \frac{\partial \eta}{\partial y'} \quad (6)$$

150 where g is the acceleration due to gravity, f is the Coriolis parameter, and η is the SLA.

151 The typhoon track data were downloaded from the Tropical Cyclone Data Center of the
 152 China Meteorological Administration (CMA). The dataset contains 6-hourly tracks and intensity
 153 analyses of typhoons that occurred in the western North Pacific from 2003 to 2020.

154

155 2.3. Shipboard sections

156 Two shipboard sections were investigated during October 2–3, 2019, and July 14–15, 2021
 157 (red and magenta points in Figure 1b). At each station, the temperature, salinity, and fluorescence
 158 profiles were collected using a Sea-Bird 911plus conductivity-temperature-depth (CTD) system.
 159 The Chl-a data from the fluorescence sensor of the CTD were not calibrated, and the signals of
 160 interest were clear.



161

162 2.4. Mapping the upwelling

163 The thermal fronts (Figure 1a) of the climatological SST in the summer stretched along the
 164 29°C isotherm. Thus, we defined the upwelling domain, i.e., core upwelling, as the area where the
 165 SST was lower than 29°C in the summer. The time series of the core upwelling area was
 166 calculated for each year during 2003–2020. Then, the time series of the Chl-a concentration in the
 167 core upwelling area for each year was obtained.

168 The upwelling index (UI) based on the wind stress is as follows:

$$169 \quad M_x = -\frac{\tau_y}{f\rho}, \quad (4)$$

170 where $\rho=1025 \text{ kg m}^{-3}$ is the water density, f is the Coriolis parameter, τ_y is the along-shelf wind
 171 stress, and M_x is the cross-shelf Ekman transport.

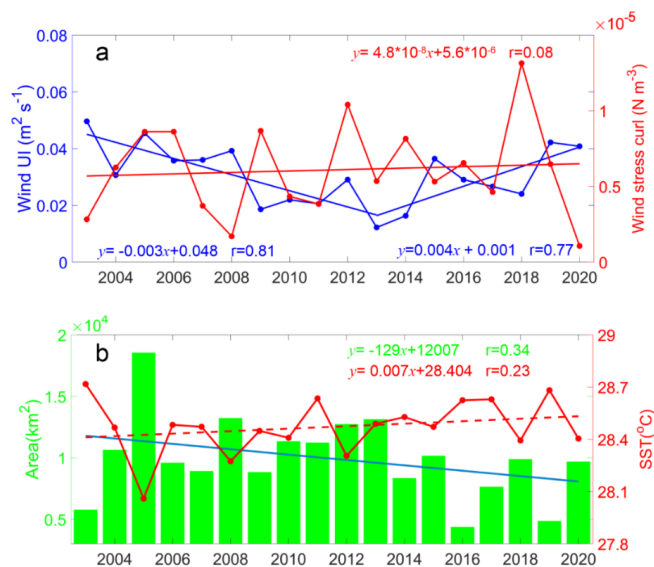
172

173 3 Chl-a concentration variations in the UEH

174 3.1 Variabilities in upwelling

175 The UI derived from the wind stress and wind stress curl are shown in Figure 2. The results
 176 reveal that the UI decreased from 2003 to 2013 and increased from 2014 to 2020, probably due to
 177 the phase switching of the Pacific Decadal Oscillation (PDO) in 2014 (Qin et al., 2018). Overall,
 178 the UI from wind stress exhibited a decreasing trend from 2003 to 2020. However, the wind stress
 179 curl exhibited a weak increasing trend from 2003 to 2020.

180



181

182 Figure 2. Upwelling index (UI) and upwelling characteristics. (a) Sea surface wind UI and wind
 183 stress curl in the study area. (b) Upwelling area and SST. In (a), the blue dotted curve denotes the
 184 UI of the wind stress during June-August; the red dotted curve is the time series of the mean wind
 185 stress curl during June-August; and the blue and red curves are the trends of the UI and wind
 186 stress curl, respectively. In (b), the green bar and red dotted curve denote the area and mean SST
 187 for the region of the study area with temperatures of less than 29°C, respectively, and the black



188 and red curves are the trends of the area and mean SST, respectively. The blue curve with squares
 189 denotes the UI of SST during June-August. The blue curve is the trend of SST UI.

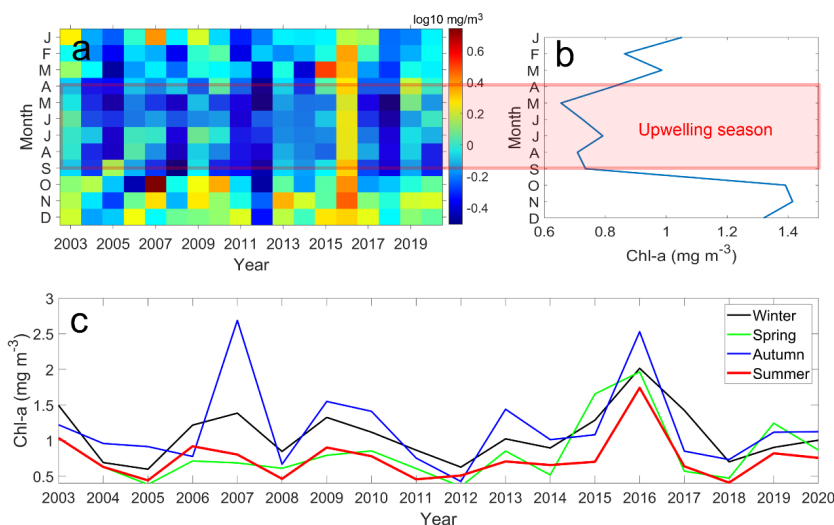
191 The area and SST of the UEH are shown in Figure 2b. The time series of the area of UEH
 192 exhibited a downward trend from 2003 to 2020. Moreover, the mean SST in the UEH exhibited an
 193 increasing trend. The trends of both the area ($-129 \text{ km}^2 \text{ y}^{-1}$) and mean SST ($0.007^\circ\text{C y}^{-1}$) indicate
 194 that the UEH gradually weakened from 2003 to 2020.

195 The time series of the UEH area and UI exhibit interannual variations. High UI values
 196 occurred in 2005, 2008, 2012, and 2015, which coincided with the large areas of upwelling in
 197 these years. Low UI values occurred in 2004, 2006, 2009, 2016 and 2019, which coincided with
 198 the small areas of upwelling in these years. The area of upwelling was small in 2003 and 2019, but
 199 peaks in the UI occurred in these years.

201 3.2. Variabilities in Chl-a concentration in the UEH

202 The time series of the spatial mean of the Chl-a concentration in the UEH is shown in Figure
 203 3. The Chl-a concentration is unexpectedly low from April to September, i.e., the upwelling
 204 season (as shown in Figures 3a-b). The climatological mean Chl-a concentration is the lowest in
 205 summer, 0.74 mg m^{-3} (as shown in Figure 3b and Table 1), which indicates the relatively limited
 206 effect of upwelling on the Chl-a concentration in the HEC. However, the mean Chl-a
 207 concentration in the UEH is highest in autumn (1.18 mg m^{-3}) and almost twice as high as that in
 208 summer. In October, the mean Chl-a concentration is as high as 1.4 mg m^{-3} .

209



210
 211 Figure 3. Time series of (a) the spatial mean of the Chl-a concentration in the upwelling area, (b)
 212 the monthly climatological mean, and (c) the seasonal mean. The red shading indicates the
 213 upwelling season from April to September.

215 Table 1. Seasonal climatologic mean Chl-a concentration in the UEH.

Period	Winter	Spring	Summer	Autumn	Annual mean
Value	1.08 ± 0.24	0.82 ± 0.44	0.74 ± 0.06	1.18 ± 0.23	0.96 ± 0.27



216
 217 The interannual variations in the spatial mean of the Chl-a concentration in the UEH are also
 218 shown in Figure 3. The Chl-a concentration in the UEH was high in 2003, 2006–2007, 2009–
 219 2010, 2013, 2015–2016 and 2019. The Chl-a concentrations in these years were 2–4 times
 220 (ranging from 1.0 to 1.8 mg m⁻³) those in the other years (2005, 2008, 2011–2012 and 2017–2018).
 221 In the remaining years, the Chl-a concentration is only approximately 0.5 mg m⁻³ in summer,
 222 which is much less than the mean value.

223 Comparing the time series of Chl-a concentration shown in Figure 3 to the time series of
 224 upwelling characteristics shown in Figure 2, one can see that low UI values coincide with high
 225 Chl-a concentration in the UEH, and vice versa. It is known that low UI values indicate weak
 226 upwelling in the HEC. This means that upwelling is a limiting factor in the UEH. Moreover, one
 227 can see that the Chl-a concentration is unexpectedly low in the upwelling season, as shown in
 228 Figures 2a–b. Therefore, the results provide new insight into the relationship between marine
 229 productivity and upwelling in the UEH. However, the effect of environmental factors and spatial
 230 variations on the Chl-a concentration need further investigation.

231 232 **4 Variations in environmental factors in the HEC**

233 **4.1 Monthly variations**

234 Figure 4 shows the climatological monthly variations in the environmental factors in the
 235 study area. As shown in Figure 4a, the mean along-shelf component of the SSW is positive from
 236 May to September, with the strongest value of 2.5 m s⁻¹ occurring in June. In the rest of the
 237 months, the along-shelf components of the SSW and wind stress curl are negative. The cross-shelf
 238 component of the SSW is also negative. The changes in the wind direction show that the study
 239 area is mainly controlled by the Asian monsoon. The period of UEH is coherent with that of the
 240 positive along-shelf wind and the wind stress curl from May to September (green shading in
 241 Figures 4a–d), indicating the effects of SSW and wind stress curl on coastal upwelling.

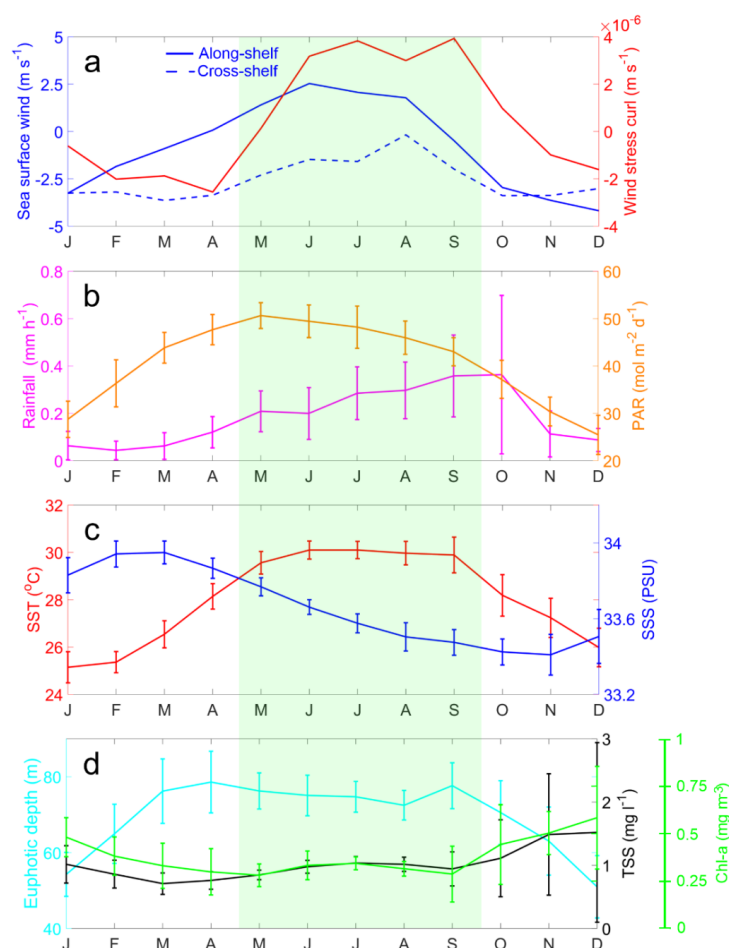


Figure 4. Monthly climatological (a) sea surface wind and wind stress curl, (b) rainfall and PAR, (c) SST and SSS, and (d) euphotic depth and TSS in the study area. The error bar indicates the standard deviation (STD). The shaded area indicates the upwelling season.

The rainfall in the study area increases monotonically from February to October and peaks in October with a value of 0.37 mm h^{-1} (Figure 4b). After October, the rainfall decreases rapidly to 0.10 mm h^{-1} in November. The rainfall in winter (December, January, and February) was less than 0.10 mm h^{-1} . Different from the rainfall, the mean photosynthetically active radiation (PAR) in the study area reaches its maximum value of $50 \text{ mol m}^{-2} \text{ d}^{-1}$ in May, indicating its dependence on the annual movement of the sun. The monthly climatological distribution of the SST is similar to that of the PAR, while the highest (lowest) SSS occurred in March (October and November) following the amount of rainfall (Figure 4c).

For the euphotic depth, the average values in the study area are greater than 50 m all year around and reach 70 m in the months of March to October (Figure 4d). In contrast, the TSS concentration is less than 1.0 mg l^{-1} from January to September and reaches the highest value of 1.5 g l^{-1} in December. Similar to the TSS, the mean Chl-a concentration in the study area has



260 smaller values of less than 0.3 mg m^{-3} from March to September, although the UEH occurs in the
261 summer months (green shading in Figure 4).

262

263 4.2 Spatial distribution

264 Figure 5 shows the spatial distributions of seasonal climatological environmental parameters.
265 The PAR is almost homogeneous in the study area (Figure 5a). The values are approximately 20–
266 $30 \text{ mol m}^{-2} \text{ d}^{-1}$ in winter, reach $50 \text{ mol m}^{-2} \text{ d}^{-1}$ in the spring and summer, and then decrease to
267 approximately $30\text{--}40 \text{ mol m}^{-2} \text{ d}^{-1}$ in autumn.

268

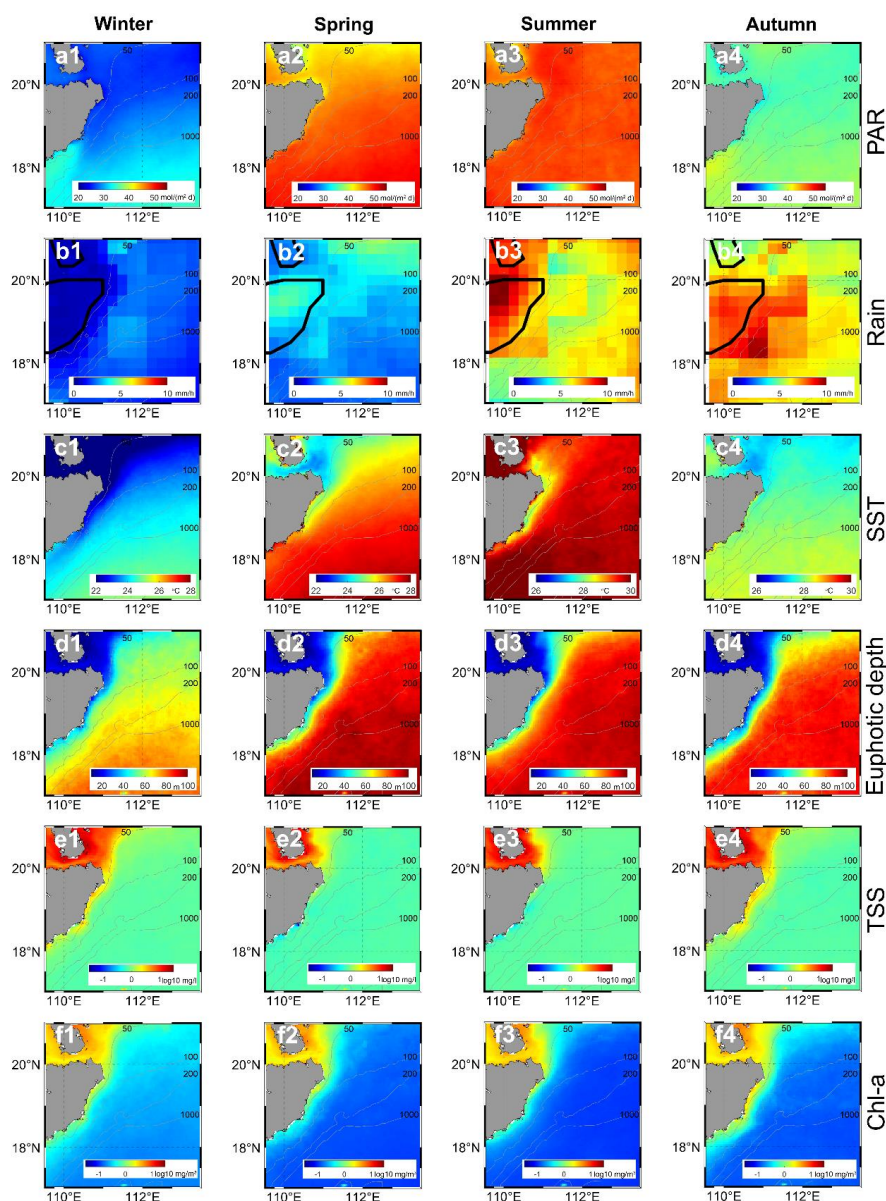


Figure 5. Seasonal climatological (a1–a4) PAR, (b1–b4) rainfall, (c1–c4) SST, (d1–d4) euphotic depth, (e1–e4) TSS, and (f1–f4) Chl-a. The columns correspond to winter, spring, summer and autumn. The unit of the numbers on the isobaths is meters.

The rainfall rate is less than 5 mm h^{-1} in winter (Figure 5b). In spring and summer, the rainfall peaks in Hainan Island, while the high precipitation area is located on Hainan Island and in the HEC area in autumn. The rainfall rate is as high as 10 mm h^{-1} in summer and autumn. Furthermore, as the high precipitation area is located on land, the heavy rain is transformed into



runoff, which carries nutrients into the sea. Thus, the temporal and spatial variations in the rainfall rate likely induce variations in the input of terrestrial materials.

The SST exhibits remarkable seasonal variability (Figure 5c). Generally, the SST is high in spring and summer and low in winter and autumn. Moreover, the SST is lower in coastal waters than in ocean areas in winter and spring, which is modulated by the prevailing southwestward current along the coastline of Guangdong (Ding et al., 2018). In summer, a region identified by low SST ($<29^{\circ}\text{C}$) values, i.e., the UEH, is observed to the northeast of Hainan Island.

The spatial distribution of the euphotic depth is consistent with the bathymetric distribution (Figure 5d). The euphotic depth in spring and summer is approximately 20–30 m within water depths of less than 50 m, whereas it is approximately 100 m in the deeper water. In winter and autumn, the euphotic depth is 20–30 m within water depths of less than 70 m. Moreover, the euphotic depth decreases to 60–80 m in the deeper water. These variations in the euphotic depth likely affect the vertical distribution of phytoplankton in the water.

Similarly, the TSS concentration is higher in the coastal area and lower in the ocean area (Figure 5e). Moreover, the TSS concentration is less than 0.3 mg l^{-1} in spring and summer in the HEC area. However, the TSS concentration increases to 3.0 mg l^{-1} at water depths of less than 70 m in autumn and winter.

The Chl-a concentration is higher in the coastal area than in the open ocean area (Figure 5f). In winter and autumn, the Chl-a concentration is higher than 1.0 mg m^{-3} at water depths of less than 70 m. In spring, the Chl-a concentration decreases to 0.5 mg m^{-3} . However, the Chl-a concentration decreases to approximately 0.3 mg m^{-3} in summer. In addition, the high concentration is approximately 1.0 mg m^{-3} in the nearshore area with water depths of less than 20 m.

4.3 EOF analysis of Chl-a concentration

To further reveal the variations in the Chl-a concentration in the HEC, the empirical orthogonal function (EOF) analysis results are shown in Figures 6–7. The first four EOF modes of the Chl-a concentration explain 60% of the total variance (Figure 6). Mode 1 includes an enhanced signal in the coastal waters ($<60\text{ m}$) to the east of Hainan Island. The magnitude of the variability is generally the same throughout the other areas. The corresponding temporal evolution (Figure 7a) is characterized by strong seasonal cycles, with peaks in October and troughs in May. The climatological mean of the corresponding temporal evolution is negative from April to September and positive from October to March. The negative phase with a large amplitude lasts for six months. Therefore, the Chl-a concentration is persistently low from April to September. Mode 1 is characterized by the GDCC (Ding et al., 2018). Mode 2 separates the east and northeast coastal waters of Hainan Island. The troughs of the temporal evolution of Mode 2 occur in September and October. The climatological mean peaks in January and December. The strong signals occur in September and October to the east of Hainan Island, which indicates that the Chl-a concentration is controlled by rainfall (as shown in Figure 5b). The other strong signals occur in January and December. Moreover, they are located on the north shelf of the SCS, adjacent to the Qiongzhou Strait to the west. Thus, the result suggests that Chl-a concentration is affected by the GDCC.

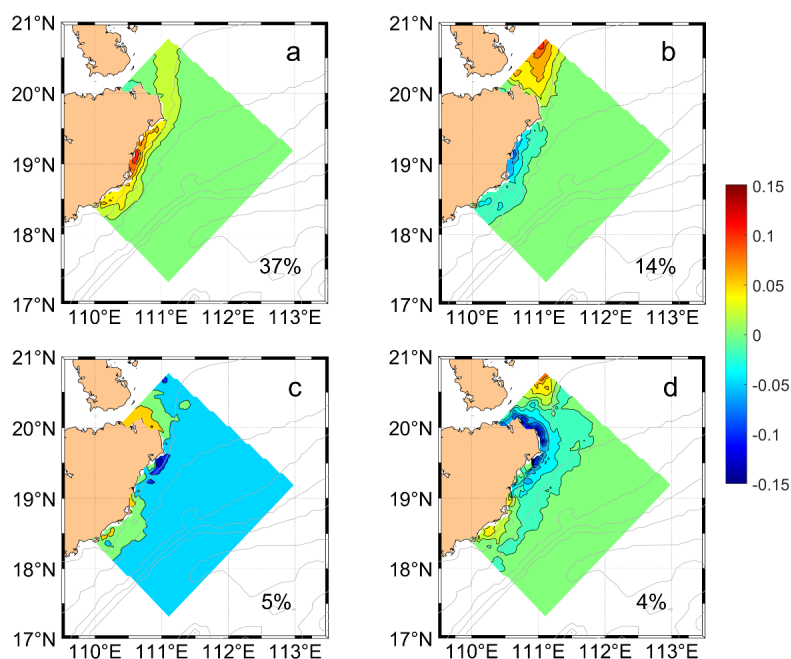


Figure 6. Spatial distributions of the first four EOFs for the Chl-a concentration. The variance explained by each mode is labeled.

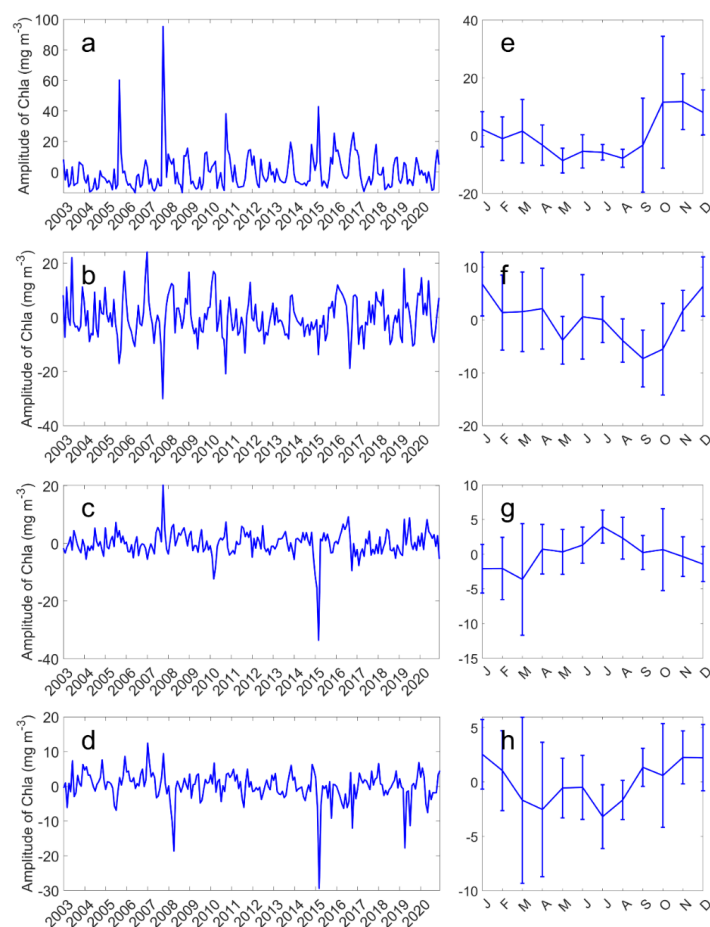


Figure 7. (a–d) Time series and (e–h) climatological mean of the first four EOFs for the Chl-a concentration.

Mode 3 describes 5% of the total variance in the Chl-a concentration in the coastal regions of Hainan Island. Mode 3 also separates the east and northeast coastal waters of Hainan Island (Figure 6c). However, the climatological mean of the temporal evolution is positive between June and August. Therefore, the positive phase occurs in summer, revealing an upwelling area to the east and north of Hainan Island. Mode 4 contributes only 4% of the total variance. The climatological mean of the temporal evolution exhibits strong peaks in July and weak peaks in April, i.e., semiannual variability. High Chl-a concentrations occur in the northeast coastal water of Hainan Island during the upwelling season.

Modes 3 and 4 both describe the upwelling phenomenon along the northeast coast of Hainan Island during summer. The spread of upwelling can be seen clearly in the EOFs of the Chl-a concentration in the areas with water depths of less than 100 m along the coastline. However, upwelling described less than 10% of the total variance in the Chl-a concentration, indicating that the contribution of upwelling to productivity in the HEC is limited.

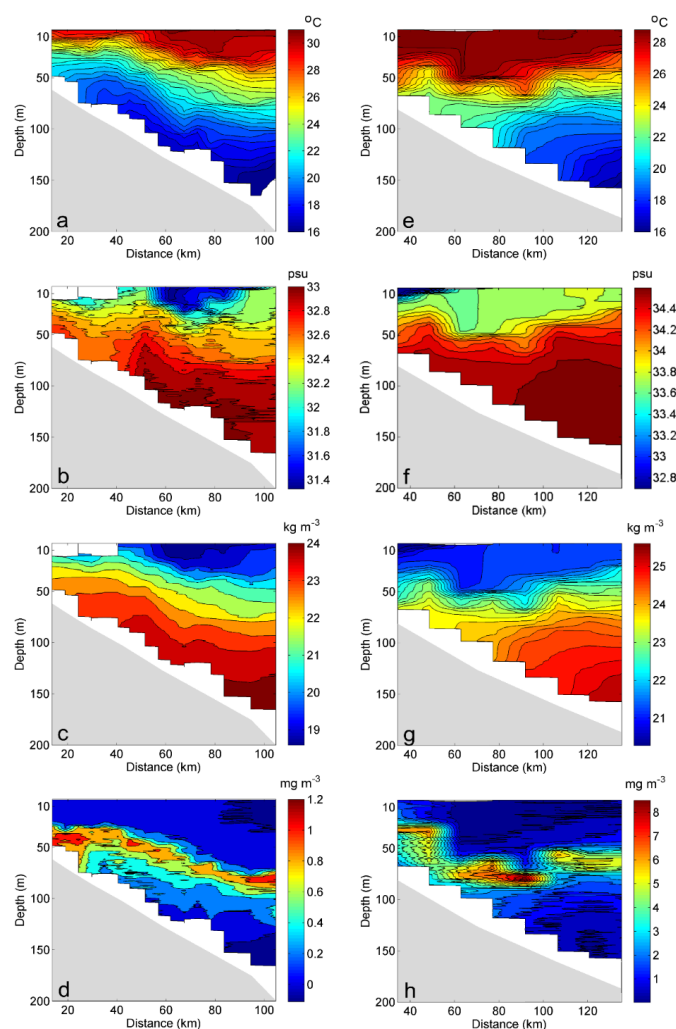


341

342 4.4 Vertical distribution of the Chl-a concentration based on observation data

343 To examine the vertical distribution of the Chl-a concentration in the HEC, two cruise
 344 measurement sections are used in this study. Figure 8 shows the oceanographic cruise data
 345 collected on July 14–15, 2021, and October 2–3, 2019, illustrating the distribution of the Chl-a
 346 concentration in summer and autumn, respectively. The pronounced upwelling can be seen on the
 347 cross-shelf section observed in July 2021. Both the isotherm and isohaline on the shelf are uplifted
 348 toward the shore by upwelling-induced movement. A temperature front can be seen near the sea
 349 surface, which is located approximately 50 km away from the coastline (depths of ~90 m). The
 350 thermal fronts are reported by Jing et al. (2016). The fronts induced by upwelling tend to be
 351 approximately aligned with the 20–100 m isobath. The high Chl-a concentration layer is also
 352 uplifted from 80 m to 40 m by upwelling, and the Chl-a concentration is as high as 1.2 mg m^{-3} .

353



354



Figure 8. Oceanographic cruise data collected on (a–d) July 14–15, 2021, and (e–h) October 2–3, 2019: a) and e) temperature distributions; b) and f) salinity distributions; c) and g) potential density distributions; and d) and h) Chl-a distributions.

From October 2–3, 2019, the sea surface temperature front disappeared. Jing et al. (2016) found that the front was the weakest in autumn. However, a salinity front occurs approximately 60 km from the coastline at a depth of ~100 m. This salinity front indicates that fresh water is injected into the sea surface. Figures 4b and 5b4 show that the rainfall is strong during autumn. The rainfall is input into the sea surface via rainfall and runoff. Thus, the salinity front is generated. In contrast to the upwelling in summer, downwelling occurs in the bottom water and is associated with downwelling-favorable wind forcing. Moreover, abundant Chl-a is detected at a depth of 30 m on the shelf, which is shallower than the detection depth in summer since the euphotic depth is shallower in autumn, as shown in Figure 5d.

5 Factors related to variations in the Chl-a concentration

5.1 Relationship with typhoon events

In the NWSCS, the Chl-a concentration can be affected by different factors, e.g., typhoons. Typhoon-induced upwelling occasionally occurs in the SCS (Ma et al., 2021; Wang et al., 2020). In the shelf areas, typhoon-enhanced vertical mixing and upwelling play dominant roles in the spatiotemporal behavior of the Chl-a concentration (Li et al., 2021a; Li et al., 2021b). The upwelling transports nutrients into the euphotic zone, which supports Chl-a blooms (Ye et al., 2013; Zheng et al., 2021). An increase in the Chl-a concentration in the nearshore region off Hainan Island followed typhoon rainfall, with mixing and upwelling effects (Zheng and Tang, 2007). The large-scale peripheral wind vector resulted in the accumulation and enhancement of the Chl-a concentration in the nearshore area (Liu et al., 2020). An offshore bloom produced a Chl-a peak (4 mg m^{-3}) after the typhoon's passage (Zheng and Tang, 2007). These observations illustrate the effects of typhoons on the marine ecosystem in the HEC.

Figure 9 shows the time series of the number of typhoons that passed over the HEC during 2003–2020. Sixty-eight typhoons passed across the continental shelf of the NWSCS during this 18-year period. There were interannual variations in the time series of the number of typhoons. As many as nine typhoons were generated and affected Qiongdong in 2013, while fewer than two typhoons passed by the study area in 2004, 2007, 2010, and 2014–2015. Seasonally, 33 typhoons passed by in summer and autumn. As shown in Figure 3b, a small peak in the mean Chl-a concentration occurred in July. Moreover, the Chl-a concentration was high in 2013, especially in autumn, varied within the range of $0.7\text{--}1.5 \text{ mg m}^{-3}$, and coincided with the occurrences of nine typhoons. This indicates that the high Chl-a concentrations were related to the typhoons. However, typhoons occur on the synoptic scale and influence the coastal area for several days. Therefore, these processes seem to have a limited effect on the monthly mean Chl-a concentration.

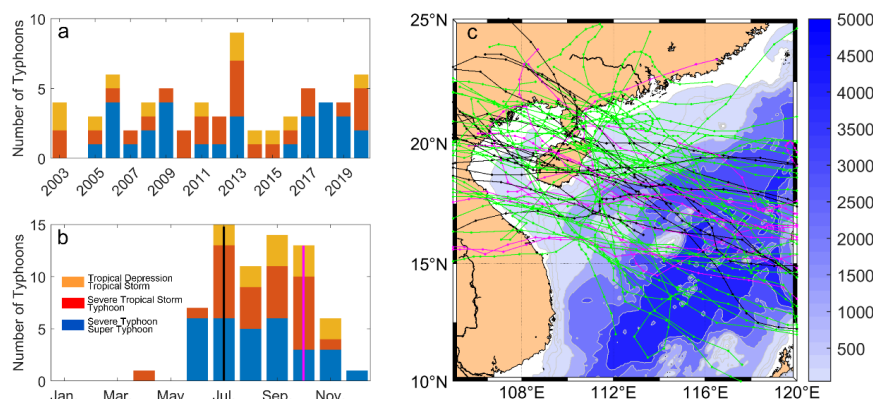


Figure 9. (a) Time series of the number of typhoons that passed by the study area during 2003–2020. (b) Seasonal distribution of typhoons. (c) Trajectories of typhoons during 2003–2020. The orange, red, and blue bars in (a–b) represent the numbers of tropical depressions and tropical storms, severe tropical storms and typhoons, and severe typhoons and super typhoons, respectively. The magenta and black curves in (c) represent the typhoons that passed by the study area in July and October, respectively. The green curves represent the typhoons that passed by the study area in the other months.

5.2 Role of the coastal current

The current in the NWSCS contributes significantly to the transport of low-salinity water, nutrients, and phytoplankton, and it also affects the ecological environment (Ding et al., 2018; Meng et al., 2017). The shelf circulation pattern is dominated by monsoons, tides, buoyancy forcing, and topography. Due to the changes in the wind direction, the current direction changes in the different seasons. In autumn and winter, the current in the NWSCS is predominantly southwestward. It changes northeastward in summer (Ding et al., 2018). The monsoon plays an important role in the current, which induces onshore and offshore Ekman transport on the shelf during the winter and summer monsoons, respectively. Gan et al. (2013) found that transport was induced by amplified geostrophic transport during downwelling events. Here, we used geostrophic current retrieval from along-track satellite altimeter data on the shelf of the NWSCS to reflect the role of the coastal current on the Chl-a concentration.

The latitudinal distribution of the climatological along-track SLA is shown in Figure 10. The climatological sea surface sloped considerably toward the ocean in October, November, and December. The sea surface on the shelf was lower than that in the ocean. The geostrophic current shows that the current was positive (northeastward) between April and August, and it was negative (southwestward) between October and March. The climatological geostrophic current in September was approximately 0 m s^{-1} , which indicates that the current direction changed frequently. The climatological geostrophic current was stronger than 0.1 m s^{-1} in summer, and it was strongest in October, at approximately 0.17 m s^{-1} .

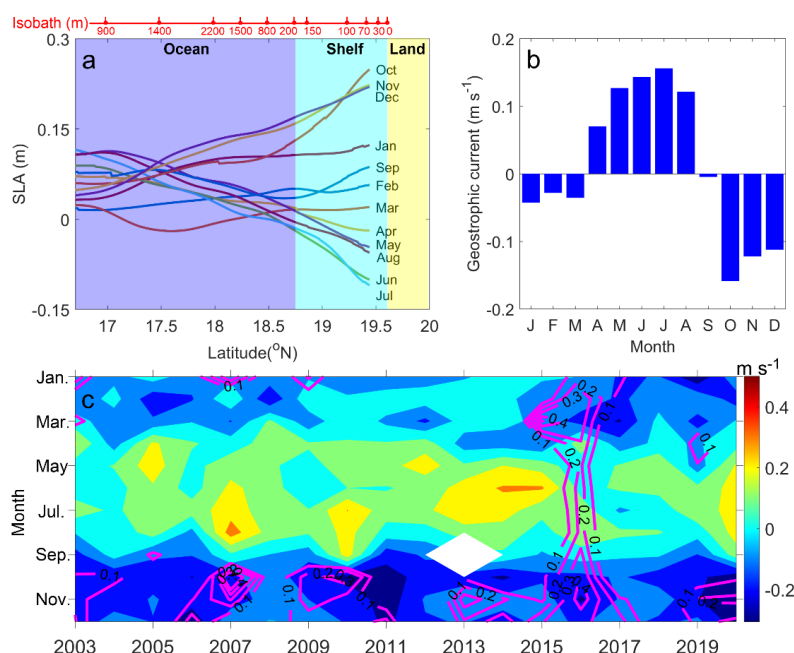


Figure 10. (a) Latitudinal distribution of climatological along-track SLA (track number: 114). (b) Geostrophic current retrieval from climatological along-track SLA. (c) Time series of geostrophic current (contours) and Chl-a concentration (magenta contour curves). The blue, cyan, and yellow shading in (a) represent the ocean, continental shelf, and land areas, respectively. The red bar with numbers in (a) indicates the water depth of the along-track SLA data. The values in (c) are the exponents of the Chl-a concentration.

In autumn and winter, the abundant nutrients in the GDCC, which were provided by the Pearl River, likely supported the high food availability to the phytoplankton (Yang and Ye, 2022). The GDCC was characterized by a high TSS (Figure 4d and 5e). TSS is synergistic with the concentration of dissolved nitrogen and is the dominant factor affecting the Chl-a concentration (López Abbate et al., 2017). The distribution of the monthly climatological Chl-a concentration (Figure 3b) was similar to that of the geostrophic current. In summer, the Chl-a concentration was low during the northeast oligotrophic current. In winter, the Chl-a concentration was high during the southwest nutrient-rich current. Figure 10c presents the time series of the geostrophic current and Chl-a concentration. The negative current and high Chl-a concentrations mainly occurred in autumn and winter, which demonstrates the crucial role of the current.

5.3 Role of rainfall

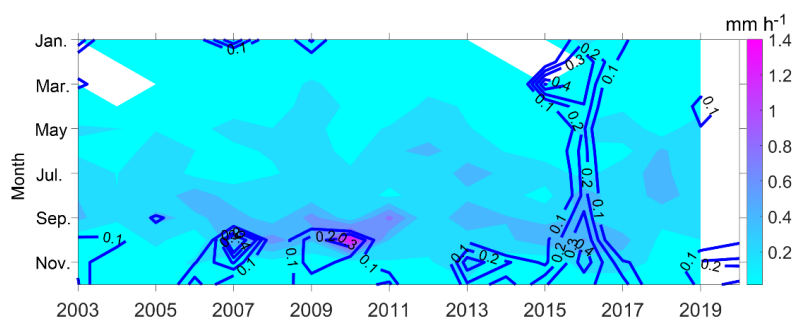
The phytoplankton responded more positively to the increased precipitation in the coastal waters (Thompson et al., 2015). Kim et al. (2014) reported that the increase in wind speed accompanied by rainfall was a major contributor to the Chl-a concentration. The precipitation directly deposits the nutrients in the air into the seawater. In addition, most of the rainfall on land runs over the land surface into the rivers and eventually into the ocean, transporting nutrients to



the ocean. Therefore, rain plays an important role in the variability of phytoplankton in coastal waters.

Figure 11 shows the time series of the monthly mean rainfall rate and Chl-a concentration. The rainfall rate was high in the summer and autumn, ranging from 0.3 to 1.4 mm h⁻¹. In October in 2007–2017, the monthly mean rainfall rate (>0.5 mm h⁻¹) coincided with the high Chl-a concentration.

455



456

Figure 11. Time series of the rainfall rate (contours) and Chl-a concentration (blue curves with text labels). The values on the contours are the exponents of the Chl-a concentration.

459

Runoff is the main source of silicate in coastal waters (Zhang et al., 2003). Chen et al. (2016) observed that the concentration of silicate was as high as 2–12 μmol l⁻¹ in the coastal waters of the HEC and had a positive correlation with the Chl-a concentration. Wang et al. (2018) found that diatoms contributed 88.11% and 85.81% of the total phytoplankton abundance in the northern SCS in May and October, respectively. The Chl-a concentration can increase by 0.3 mg·m⁻³ after a rainfall event (Zeng et al., 2022). Moreover, in Mode 2 of the EOFs (Figures 6–7), the positive phase of the Chl-a concentration occurred off the east coast of Hainan Island in October, which is near the estuary of the Wanquan River. Therefore, the runoff caused by the high rainfall rate triggered the high Chl-a concentrations in the HEC.

469

5.4 Relationship with ENSO events

470

ENSO has an indirect positive effect on the Chl-a concentration through its influences on precipitation, winds, SST, and turbidity (López Abbate et al., 2017). In the SCS, easterly wind anomalies and SST warming occurred in the summer following El Niño events (Yang et al., 2015). During El Niño events, the weakened southwesterly monsoon suppresses ocean upwelling (Jing et al., 2011; Kuo et al., 2008). The reverse occurs during La Niña events. Jing et al. (2011) found that the significantly strengthened wind stress of the 1998 summer induced strong upwelling, and the Chl-a concentration was much higher than in any of the other years.

478

In the upwelling season, i.e., summer, the wind stress was smaller during El Niño events (Table 2) than during La Niña events (Figure 2a). The Chl-a concentration in July during El Niño events increased to as high as 1.0 mg m⁻³ (Figure 3a). Moreover, the SST of the core upwelling area was higher, but the core area was smaller (Figure 2b). Therefore, ENSO events regulated the Chl-a concentration of the upwelling through wind stress.

483



Table 2. ENSO events during 2003–2020.

ENSO event	Years
El Niño	2003, 2004, 2006, 2009, 2015, 2019
La Niña	2005, 2007–2008, 2010–2012, 2016, 2017–2018

In autumn, especially October, the spatial mean Chl-a concentration in the upwelling area was as high as $1.18 \pm 0.23 \text{ mg m}^{-3}$. The precipitation was heavier during La Niña events (i.e., in 2005, 2007, 2010–2011, and 2016) than during El Niño events. Furthermore, the along-shelf current from the north was crucially important to the Chl-a concentration. There was a positive relationship between the Chl-a anomalies and the La Niña events.

5.5 Mechanisms of Chl-a variations in the HEC area

Figure 12 shows the relationships between the geostrophic current and rainfall and the Chl-a concentration during 2003–2020. The Chl-a concentration increased with increasing rainfall in August, i.e., the upwelling season. The rainfall was converted to runoff and flowed into the coastal waters. The Chl-a concentration in summer was mainly regulated by upwelling processes (Jing et al., 2011), with a negative correlation (Figures 2–3). Therefore, the increased precipitation and weaker upwelling processes could have induced the increased Chl-a concentration in the HEC (upward arrow in Figure 12).

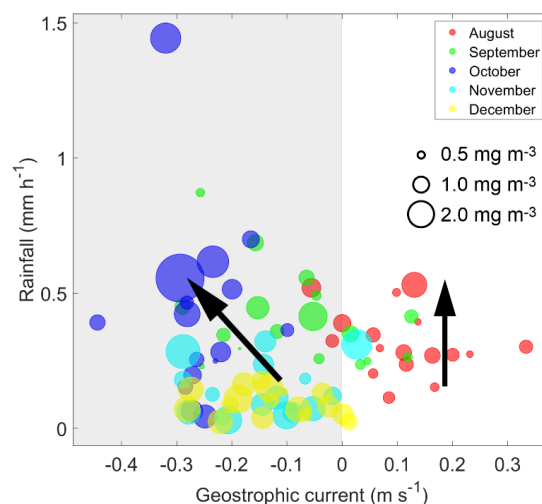


Figure 12. Bubble diagram showing the relationships between the geostrophic current and rainfall and the Chl-a concentration. The size of the bubble represents the Chl-a concentration. The left panel in grey represents the southwest along-shelf current in winter. The right panel represents the northeast along-shelf current in summer. Black arrows represent the relationship between the geostrophic current and rainfall and the Chl-a concentration.

In autumn and winter, the Chl-a concentration was increased by the increases in rainfall and



the northeastward coastal current (oblique upward arrow in Figure 12). In October, the heaviest rainfall and the strongest current coincided with the highest Chl-a concentration. The coastward wind component was strongest in October (Figure 4a), as was the northeast monsoon, which induced coastward Ekman transport (Xuan et al., 2021). The downwelling movement transported the nutrients from the rivers and the coastal current to the middle and under layers on the shelf, which promoted an increase in silicate-favoring phytoplankton. The cruise data provide evidence of the high Chl-a concentrations over the shelf (Figure 8h).

6 Conclusions

In this study, in situ observations and monthly satellite observations from 2003 to 2020 are used to investigate the spatiotemporal variability in the Chl-a concentration in the HEC area. Along-track satellite altimeter data for the continental shelf of the NWSCS were used to retrieve the geostrophic current. In addition, cruise data obtained in October 2019 and July 2021 were used to examine the vertical structure of the Chl-a concentration during the three observational seasons.

Driven by the prevailing monsoon, the SST of the core upwelling area (within a depth of 100 m) in summer increased, but its area decreased, which indicates that the UEH weakened during the 18-year study period. The EOF analysis of the Chl-a concentration revealed that it exhibited strong seasonal and interannual variability in the NWSCS. The climatological average Chl-a concentration mostly peaked near the coast in autumn, 1.18 mg m^{-3} . However, the Chl-a concentration in the core upwelling area was lowest during the upwelling season, approximately 0.74 mg m^{-3} in summer, which contradicts the previous conclusion of a high-productivity upwelling system.

ENSO events regulated the Chl-a concentration of the upwelling area through wind stress. The interannual variations in the spatial mean of the Chl-a concentration were consistent with the ENSO events. There was a positive correlation between the Chl-a anomalies and the La Niña events. In El Niño years, the Chl-a concentration decreased to a lower level in summer. However, the summer Chl-a concentration increases to as high as 1.0 mg m^{-3} with weak upwelling during El Niño years.

Both the along-shelf current from the north and precipitation were crucial factors controlling the Chl-a concentration in the UEH area. The downwelling movement transported nutrients from the rivers and the coastal current to the middle and lower layers on the shelf, which promoted an increase in silicate-favoring phytoplankton. These results provide scientific evidence for the development of the marine economy in the upwelling area.

Acknowledgments

The authors are grateful to the anonymous reviewers for their valuable suggestions and comments. This research was funded by the National Natural Science Foundation of China (41476009, 41506018, 41976200, 41706025); Innovation Team Plan for Universities in Guangdong Province (2019KCXTF021); and First-class Discipline Plan of Guangdong Province (080503032101, 231420003).

Data Availability Statement

Kd490, Rrs645, Chl-a, SST, and PAR data were downloaded from Ocean Color Data Processing System (<http://oceandata.sci.gsfc.nasa.gov/>)



SSW, SSS, rainfall rate, and along-track SLA data were downloaded from CMEMS
 (<https://marine.copernicus.eu/>)
 The shipboard sections data are archived at <https://dx.doi.org/10.6084/m9.figshare.19679538>.
 The typhoon track was obtained from the Tropical Cyclone Data Center of the China
 Meteorological Administration (CMA) (<http://tcdata.typhoon.org.cn>).

Author contributions

JYL, ML and LLX were responsible for writing the original draft. Review and editing were
 conducted by QAZ. Conceptualization was handled by JYL, QAZ and LLX. CW, YX and TYZ
 were responsible for data curation. LLX acquired funding.

Competing interests

The contact author has declared that none of the authors has any competing interests.

Disclaimer

Publisher's note: Copernicus Publications remains neutral with regard to jurisdictional claims in
 published maps and institutional affiliations.

References

- Aoki, K., Kuroda, H., Setou, T., Okazaki, M., Yamatogi, T., Hirae, S., Ishida, N., Yoshida, K., Mitoya,
 Y., 2019. Exceptional red-tide of fish-killing dinoflagellate *Karenia mikimotoi* promoted by typhoon-
 induced upwelling. *Estuarine Coastal and Shelf Science* 219, 14-23.
- Barua, D.K., 2005. Coastal Upwelling and Downwelling, in: Schwartz, M.L. (Ed.), *Encyclopedia of*
Coastal Science. Springer Netherlands, Dordrecht, pp. 306-308.
- Cape, M.R., Straneo, F., Beaird, N., Bundy, R.M., Charette, M.A., 2019. Nutrient release to oceans
 from buoyancy-driven upwelling at Greenland tidewater glaciers. *Nature Geoscience* 12, 34-39.
- Chen, F., Zhen, Z., Meng, Y., Zhu, Q., Xie, L., Zhang, S., Chen, Q., Chen, J., 2016. Diel variation of
 nutrients and chlorophyll α concentration in the Qiongdong sea region during the summer of 2013.
Haiyang Xuebao 38, 76-83.
- Deng, S., Zhong, H., Wang, M., Yun, F., 1995. On relation between upwelling off Qionghai and fishery.
Journal of Oceanography In Taiwan Strait 14, 51-56.
- Ding, Y., Yao, Z., Zhou, L., Bao, M., Zang, Z., 2018. Numerical modeling of the seasonal circulation in
 the coastal ocean of the Northern South China Sea. *Frontiers of Earth Science* 14, 90-109.
- Gan, J., San Ho, H., Liang, L., 2013. Dynamics of Intensified Downwelling Circulation over a
 Widened Shelf in the Northeastern South China Sea. *Journal of Physical Oceanography* 43, 80-94.
- Hu, J., Wang, X.H., 2016. Progress on upwelling studies in the China seas. *Reviews of Geophysics* 54,
 653– 673.
- Hu, Q., Chen, X., Huang, W., Zhou, F., 2021. Phytoplankton bloom triggered by eddy-wind interaction
 in the upwelling region east of Hainan Island. *Journal of Marine Systems* 214, 103470.
- Jing, Z., Qi, Y., Du, Y., 2011. Upwelling in the continental shelf of northern South China Sea associated
 with 1997-1998 El Nino. *Journal of Geophysical Research* 116, C02033.
- Jing, Z., Qi, Y., Du, Y., Zhang, S., Xie, L., 2015. Summer upwelling and thermal fronts in the
 northwestern South China Sea: Observational analysis of two mesoscale mapping surveys. *Journal of*
Geophysical Research: Oceans 120, 1993-2006.



- 597 Jing, Z., Qi, Y., Fox-Kemper, B., Du, Y., Lian, S., 2016. Seasonal thermal fronts on the northern South
598 China Sea shelf: Satellite measurements and three repeated field surveys. *Journal of Geophysical*
599 *Research: Oceans* 121, 1914-1930.
- 600 Jing, Z., Qi, Y., Hua, Z.-l., Zhang, H., 2009. Numerical study on the summer upwelling system in the
601 northern continental shelf of the South China Sea. *Continental Shelf Research* 29, 467-478.
- 602 Kim, T.-W., Najjar, R.G., Lee, K., 2014. Influence of precipitation events on phytoplankton biomass in
603 coastal waters of the eastern United States. *Global Biogeochemical Cycles* 28, 1-13.
- 604 Kuo, N., Ho, C., Lo, Y., Huang, S., Tsao, C., 2008. Variability of chlorophyll-a concentration and sea
605 surface wind in the South China Sea associated with the El Niño-Southern Oscillation, *OCEANS 2008*
606 - MTS/IEEE Kobe Techno-Ocean, pp. 1-5.
- 607 López Abbate, M.C., Molinero, J.C., Guinder, V.A., Perillo, G.M.E., Freije, R.H., Sommer, U., Spetter,
608 C.V., Marcovecchio, J.E., 2017. Time-varying environmental control of phytoplankton in a changing
609 estuarine system. *Science of The Total Environment* 609, 1390-1400.
- 610 Li, J., Zheng, H., Xie, L., Zheng, Q., Ling, Z., Li, M., 2021a. Response of Total Suspended Sediment
611 and Chlorophyll-a Concentration to Late Autumn Typhoon Events in the Northwestern South China
612 Sea. *Remote Sensing* 13, 2863.
- 613 Li, J., Zheng, Q., Hu, J., Xie, L., Zhu, J., Fan, Z., 2016. A case study of winter storm-induced
614 continental shelf waves in the northern South China Sea in winter 2009. *Continental Shelf Research*
615 125, 127-135.
- 616 Li, J., Zheng, Q., Li, M., Li, Q., Xie, L., 2021b. Spatiotemporal Distributions of Ocean Color Elements
617 in Response to Tropical Cyclone: A Case Study of Typhoon Mangkhut (2018) Past over the Northern
618 South China Sea. *Remote Sensing* 13, 687.
- 619 Lin, P., Cheng, P., Gan, J., Hu, J., 2016. Dynamics of wind-driven upwelling off the northeastern coast
620 of Hainan Island. *Journal of Geophysical Research: Oceans* 121, 1160-1173.
- 621 Liu, S.H., Li, J.G., Sun, L., Wang, G.H., Tang, D.L., Huang, P., Yan, H., Gao, S., Liu, C., Gao, Z.Q., Li,
622 Y.B., Yang, Y.J., 2020. Basin-wide responses of the South China Sea environment to Super Typhoon
623 Mangkhut (2018). *Science of the Total Environment* 731, 139093.
- 624 Liu, Y., Peng, Z., Shen, C.-C., Zhou, R., Song, S., Shi, Z., Chen, T., Wei, G., DeLong, K.L., 2013.
625 Recent 121-year variability of western boundary upwelling in the northern South China Sea.
626 *Geophysical Research Letters* 40, 3180-3183.
- 627 Ma, C., Zhao, J., Ai, B., Sun, S., 2021. Two-Decade Variability of Sea Surface Temperature and
628 Chlorophyll-a in the Northern South China Sea as Revealed by Reconstructed Cloud-Free Satellite
629 Data. *IEEE Transactions on Geoscience and Remote Sensing* 59, 9033-9046.
- 630 McGregor, H.V., Dima, M., Fischer, H.W., Mulitza, S., 2007. Rapid 20th-Century Increase in Coastal
631 Upwelling off Northwest Africa. *Science* 315, 637-639.
- 632 Meng, F., Dai, M., Cao, Z., Wu, K., Zhao, X., Li, X., Chen, J., Gan, J., 2017. Seasonal Dynamics of
633 Dissolved Organic Carbon Under Complex Circulation Schemes on a Large Continental Shelf: The
634 Northern South China Sea. *Journal of Geophysical Research: Oceans* 122, 9415-9428.
- 635 Ning, X., Chai, F., Xue, H., Cai, Y., Liu, C., Shi, J., 2004. Physical-biological oceanographic coupling
636 influencing phytoplankton and primary production in the South China Sea. *Journal of Geophysical*
637 *Research: Oceans* 109.
- 638 Qin, M., Li, D., Dai, A., Hua, W., Ma, H., 2018. The influence of the Pacific Decadal Oscillation on
639 North Central China precipitation during boreal autumn. *International Journal of Climatology* 38, 821-
640 831.



- 641 Shi, W., Huang, Z., Hu, J., 2021. Using TPI to Map Spatial and Temporal Variations of Significant
642 Coastal Upwelling in the Northern South China Sea. *Remote Sensing* 13, 1065.
- 643 Song, X., Lai, Z., Ji, R., Chen, C., Zhang, J., Huang, L., Yin, J., Wang, Y., Lian, S., Zhu, X., 2012.
644 Summertime primary production in northwest South China Sea: Interaction of coastal eddy, upwelling
645 and biological processes. *Continental Shelf Research* 48, 110-121.
- 646 Su, J., Xu, M.Q., Pohlmann, T., Xu, D.F., Wang, D.R., 2013. A western boundary upwelling system
647 response to recent climate variation (1960-2006). *Continental Shelf Research* 57, 3-9.
- 648 Thompson, P.A., O'Brien, T.D., Paerl, H.W., Peierls, B.L., Harrison, P.J., Robb, M., 2015. Precipitation
649 as a driver of phytoplankton ecology in coastal waters: A climatic perspective. *Estuarine, Coastal and*
650 *Shelf Science* 162, 119-129.
- 651 Wang, C., Wang, W., Wang, D., Wang, Q., 2006. Interannual variability of the South China Sea
652 associated with El Niño. *Journal of Geophysical Research: Oceans* 111.
- 653 Wang, L., Xie, L., Zheng, Q., Li, J., Li, M., Hou, Y., 2020. Tropical cyclone enhanced vertical transport
654 in the northwestern South China Sea I: Mooring observation analysis for Washi (2005). *Estuarine,*
655 *Coastal and Shelf Science* 235, 106599.
- 656 Wang, Y., Kang, J.-h., Liang, Q.-y., He, X.-b., Wang, J.-j., Lin, M., 2018. Characteristics of
657 phytoplankton communities and their biomass variation in a gas hydrate drilling area in the northern
658 South China Sea. *Marine Pollution Bulletin* 133, 606-615.
- 659 Xie, L., Zhang, S., Zhao, H., 2012. Overview of studies on Qiongdong upwelling. *Journal of Tropical*
660 *Oceanography*, 38-44.
- 661 Xu, D., Huang, H., Zheng, N., Zhang, J., Pan, A., 2020. Role of biological activity in mediating
662 acidification in a coastal upwelling zone at the east coast of Hainan Island. *Estuarine Coastal and Shelf*
663 *Science* 249.
- 664 Xuan, J., Ding, R., Ni, X., Huang, D., Chen, J., Zhou, F., 2021. Wintertime Submesoscale Offshore
665 Events Overcoming Wind-Driven Onshore Currents in the East China Sea. *Geophysical Research*
666 *Letters* 48, e2021GL095139.
- 667 Yang, C., Ye, H., 2022. Enhanced Chlorophyll-a in the Coastal Waters near the Eastern Guangdong
668 during the Downwelling Favorable Wind Period. *Remote Sensing* 14, 1138.
- 669 Yang, Y., Xie, S.-P., Du, Y., Tokinaga, H., 2015. Interdecadal Difference of Interannual Variability
670 Characteristics of South China Sea SSTs Associated with ENSO. *Journal of Climate* 28, 7145-7160.
- 671 Ye, H.J., Sui, Y., Tang, D.L., Afanasyev, Y.D., 2013. A subsurface chlorophyll a bloom induced by
672 typhoon in the South China Sea. *Journal of Marine Systems* 128, 138-145.
- 673 Zeng, D., Li, J., Xie, L., Ye, X., Zhou, D., 2022. Analysis of temporal characteristics of chlorophyll a in
674 Lingding Bay during summer. *Journal of Tropical Oceanography* 41, 16-25.
- 675 Zhang, J., Ren, J.L., Liu, S.M., Zhang, Z.F., Wu, Y., Xiong, H., Chen, H.T., 2003. Dissolved aluminum
676 and silica in the Changjiang (Yangtze River): Impact of weathering in subcontinental scale. *Global*
677 *Biogeochemical Cycles* 17, 1077.
- 678 Zhao, J., Barnes, B., Melo, N., English, D., Lapointe, B., Muller-Karger, F., Schaeffer, B., Hu, C.,
679 2013. Assessment of satellite-derived diffuse attenuation coefficients and euphotic depths in south
680 Florida coastal waters. *Remote Sensing of Environment* 131, 38-50.
- 681 Zheng, G.M., Tang, D.L., 2007. Offshore and nearshore chlorophyll increases induced by typhoon
682 winds and subsequent terrestrial rainwater runoff. *Marine Ecology Progress Series* 333, 61-74.
- 683 Zheng, M., Xie, L., Zheng, Q., Li, M., Chen, F., Li, J., 2021. Volume and Nutrient Transports Disturbed
684 by the Typhoon Chebi (2013) in the Upwelling Zone East of Hainan Island, China. *Journal of Marine*



685 Science and Engineering 9, 324.

686

687

688